Article

Vortex of a Symmetric Jet Structure in a Natural Gas Pipeline via Proper Orthogonal Decomposition

Lihao Li [1,2,3], Jiaxing Lu [1,2,3,*], Haoyu Zhao [1,2,3] and Yilong Qiu [4]

1   Key Laboratory of Fluid and Power Machinery, Ministry of Education, Xihua University,
     Chengdu 610039, China; leolineo@163.com (L.L.); 17361345933@163.com (H.Z.)
2   School of Energy and Power Engineering, Xihua University, Chengdu 610039, China
3   Key Laboratory of Fluid Machinery and Engineering, Xihua University, Chengdu 610039, China
4   Natural Gas Research Institute, PetroChina Southwest Oil & Gas Field Company, Chengdu 610213, China;
     qiuyilong@petrochina.com.cn
*   Correspondence: jiaxinglu@mail.xhu.edu.cn

Abstract: The impact of particle addition jets on the flow field in natural gas pipelines was investigated, and the structural information of the flow field at different flow velocities in a symmetric jet flow was analyzed via numerical simulation. The results of coherent structures in the high-pressure natural gas pipeline reveal vortex structures of varying sizes both upstream and downstream of the jet flow. To determine the spatial distribution of the main vortex structures in the flow field, proper orthogonal decomposition (POD) mode analysis was performed on the unsteady numerical results. Moreover, the detailed spatial characteristics of the coherent vortex structures represented by each mode were obtained. The results indicate that the large-scale vortex structures within the pipeline are balanced and stable, with their energy increasing as the jet flow velocity increases. Additionally, higher-order modes exhibit significant shedding of small-scale vortex structures downstream of the jet flow. In this research, coherent structures present in symmetric particle addition jets are provided, offering theoretical support for future investigations on the distribution of particle image velocimetry (PIV) flowmeters.

Keywords: jet flow; numerical simulation; POD; natural gas; coherent structure

1. Introduction

Natural gas is an invisible, odorless, and nonrenewable gas mixture, with methane being the major component, accounting for approximately 95% of its composition [1]. Its development and utilization have the potential to generate substantial economic benefits. Natural gas is commonly regarded as a fossil fuel with comparatively low environmental impact, and its use can contribute to environmental quality to some extent. As global concerns about environmental issues continue to grow, the significance of natural gas is anticipated to become increasingly prominent [2–5]. Currently, global natural gas consumption is gradually increasing. The next 15 years are anticipated to witness a continued surge in China's demand for natural gas, and it is estimated that natural gas consumption will reach a peak at approximately 2040, at 6100×10^8 cubic meters [6–8]. As the demand for natural gas on the market continues to grow, it is necessary for the market to optimize the natural gas system and transform natural gas pipeline measurement technology. PIV technology employs the scattering properties of particles in a flow field to track their positions and measure their displacement at different time intervals, thereby enabling the determination of flow velocity and other related parameters [9,10]. PIV technology is playing an increasingly important role in experimental fluid dynamics because of its noninvasive measurement characteristics. Compared with traditional measurement techniques, PIV does not interfere with the flow field, making it advantageous in many fluid experiments [11]. Li et al. [12] argue that PIV technology offers benefits such as resistance

to interference and ease of installation. Additionally, they proposed innovative ideas for its application in the measurement of flow fields and developed the PIV flowmeter. However, the distribution of tracer particles in pipeline flow fields is affected by coherent jet vortices, and this principle is not explained in detail. The distribution of particles will affect the accuracy of a PIV flowmeter.

The achievements of computational fluid dynamics (CFD) since the 1970s have demonstrated the powerful vitality of these methods for the study of various fluid phenomena and industrial and engineering applications [13]. Currently, relatively few CFD analyses of symmetric jets exist. Atmaca et al. [14] studied the jets emitted by three different slot nozzles and predicted the free jet velocity at different axial distances. Muhammad et al. [15] used an LES model to study turbulent kinetic energy. Kinetic energy is calculated at the inlet and outlet of turbulent flow. Rehman et al. [16] studied the flow characteristics of a micropolar-Casson fluid, which is doubly stratified and induced by a stretching sheet, their findings are highly consistent with existing results in the literature for specific scenarios. Cao et al. [17] used a new computational method to model the flow of nanofluids in a cavity with a corrugated inner wall with uniform flux. Upadhyay et al. [18] studied the flow and acoustic characteristics of rectangular and elliptical asymmetric jets and compared them with the equivalent area of circular jets. Xiao et al. [19] established a single-nozzle model with different transverse velocities and studied the characteristics of jet flow fields and deflection. Cai et al. [20] developed a two-dimensional computational fluid dynamics (CFDs) model to investigate the flow structure of a liquid nitrogen jet and conducted numerical simulations to analyze the transient velocity and temperature distribution of the jet. Their findings clearly demonstrate that the liquid nitrogen jet exhibits distinct regions, including a velocity boundary and potential core region, which are similar to those observed in water jets. Bi et al. [21] conducted numerical simulations to investigate the characteristics of human cough jets in a calm environment, including the temporal evolution of the velocity distribution, the penetration distance along the jet axis, and the maximum width of the jet. Their findings demonstrate that employing LES methodology enables accurate prediction of the temporal development of a human cough jet. Hou et al. [22] investigated the flow field of an ultrahigh-pressure waterjet (WJ) with high-frequency velocity vibration at the nozzle inlet using computational fluid dynamics. They successfully obtained the velocity field inside the nozzle and examined how various vibration parameters, such as amplitude and frequency, affect the flow field. Their simulation results revealed significant changes in the flow field, corresponding to different frequencies and amplitudes. Lee et al. [23] investigated the three-dimensional density distribution of twin jets through numerical simulations and experimental studies. Their findings revealed that the interaction between the twin jets led to an increase in density within the shear layer located between the nozzles, while both increasing and decreasing interference trends were observed. Furthermore, they noted variations in both the initiation point and growth rate of this interaction phenomenon. Hart et al. [24] performed numerical simulations to investigate the dynamic flow characteristics of oblique-opening rectangular jets and examined the issue of vortex shedding in a cluster of three rectangular burner jets. Their findings indicated that the combination of an adverse pressure gradient, caused by the recess's diffuser-like shape, and fluid entrainment into the gaps between the jets led to the occurrence of vortex shedding. Miltner et al. [25] conducted an extensive examination of the flow characteristics of a turbulent free jet, both through experimental analysis and computational fluid dynamics (CFDs) simulation, using different turbulence models. The findings indicated that numerical simulation proved to be an effective method for precisely characterizing the investigated flow pattern. Zheng et al. [26] investigated the interaction of three jets that were aligned in a single plane and converged towards each other. A particle image velocimetry system was employed to capture the flow fields, facilitating analysis and characterization of the intricate flow patterns on two perpendicular planes based on velocity and vorticity distributions.

CFDs simulations can be conducted for a low cost, have short cycles, and high efficiency. Scholars at home and abroad have used this approach to conduct in-depth research

on the internal flow of pipelines [27,28]. Therefore, in this article, unsteady numerical simulations on the symmetric jet flow field of high-pressure natural gas and pipelines have been performed, and the research focuses on investigating the flow properties of natural gas within symmetric jet flow conditions. Among them, the jet has a significant influence on the internal flow field of natural gas, which makes the flow field structure more complex, and it is necessary to reduce the order of the flow field to extract a smooth feature structure from several datasets. Proper orthogonal decomposition (POD) can be employed to effectively reduce the dimensionality of intricate high-dimensional systems [29]. Currently, the POD method is also widely used in the field of computational fluid dynamics. Daichin et al. [30] utilized the POD method to analyze the motion of the near wake behind an elliptic cylinder positioned beneath a free surface. The findings indicated that the first four eigenmodes provide insights into the overall flow structure, with the large-scale structure being related mainly to the most energetic flow motion. Sakai et al. [31] conducted investigations on the velocity fields surrounding a circular cylinder by employing the POD and DMD methods. Both experimentally and numerically, the experimental findings indicated that there was general consistency between the flow structures observed in the POD and DMD modes compared to those obtained through numerical simulations. EI-Adawy et al. [32] employed stereo-PIV to acquire velocity vector fields for in-cylinder flow under various experimental conditions. They utilized the POD method to analyze synthetic velocity vector fields with known characteristics and discovered that, in the case of repeatable flow patterns, only the first mode was adequate for reconstructing the physical properties of the flow. Zhang et al. [33] utilized the large eddy simulation (LES) method to numerically simulate a three-dimensional incompressible flow of an annular jet at a Reynolds number of 8500. The velocity fluctuation vectors were subjected to proper orthogonal decomposition (POD) analysis to investigate the flow dynamics of the wake flow. The findings indicate that the asymmetrical mean flow observed near the annular jet is associated with the first two POD modes, which correspond to a significant displacement in the stagnation point. Jang et al. [34] investigated the flow properties of a turbulent wake formed behind a sphere in a subcritical flow regime. Detailed flow information was obtained using particle image velocimetry measurements and POD modal analysis techniques. Deep et al. [35] investigated the occurrence of vortex shedding in the wake of a circular cylinder and examined how attaching a splitter plate to the rear stagnation point affects this flow phenomenon. Wang et al. [36] employed the LES model to conduct numerical simulations on three typical setups of tornado-like vortices. They also performed POD decomposition on the flow field and observed that the conditional average reveals more significant coherent structures at larger scales compared to the conventional ensemble average. Wu et al. [37] conducted computational fluid dynamics (CFDs) simulations on a horizontal axis wind turbine and analyzed the data using an extended proper orthogonal decomposition (POD) algorithm. The quantitative findings suggest that the wake's tip vortex exhibits a complex spatiotemporal morphological configuration in the higher-order extended POD space, while also confirming the effectiveness and reliability of the obtained radial velocity modes. In addition, Apacoglu et al. [38] conducted a computational analysis on the flow patterns over a two-dimensional circular cylinder and its control through air blowing from various slots positioned on the surface of the cylinder. The POD method was employed to categorize flow structures based on their frequency content. Additionally, an optimal selection of sensor locations on the cylinder surface was determined by employing a one-dimensional POD analysis using surface pressure data obtained from CFD results. Sen et al. [39] conducted a numerical simulation to analyze unsteady two-dimensional laminar fluid flow around a circular cylinder. They qualitatively investigated how changes in the injected stream velocity affected the downstream wake region of the cylinder. Additionally, they utilized proper orthogonal decomposition to identify and quantify dominant modes within the vorticity field, including their corresponding enstrophy contents.

　　In this article, CFDs is utilized to numerically simulate a high-pressure natural gas pipeline in a multiple-pipe symmetrical injection system. The evolution of vortex structures

under different flow velocities of the jet is analyzed, and the study investigates the impact of symmetric injection on the internal flow characteristics of natural gas. The unsteady numerical simulation results are subjected to POD mode analysis, enabling an examination of the flow patterns associated with each mode. A computational approach is employed for conducting the simulations.

2. Numerical Simulation Method

2.1. Numerical Model

In this study, Unigraphics NX was used to create a 1:1 model of the natural gas pipeline, and the outlet of a natural gas pipeline was extended, as shown in Figure 1. The Y+ value of the tube wall is between 30 and 100. The natural gas test system consists of a natural gas main pipeline and four tracer particle injection pipelines, the parameters of which are shown in Table 1. ICEM V14.5 software was used to divide the pipeline model into hexahedral structural grids, and CFX was used to conduct a numerical simulation of the flow field inside the pipeline, as shown in Figure 2. The standard k-epsilon model was used for numerical simulation to simulate the steady-state and transient conditions, and the fluid material was set as methane gas at 1.5 MPa. The initial condition of the transient file is a stable steady-state file, and the unsteady-state flow rate is calculated with a step size of 0.01 s. On this basis, to calculate another 50 steps, the intermediate file was used to calculate the POD. The direction of gravity is shown in Figure 1. The boundary conditions were set as the flow inlet and pressure outlet. The inlet flow rate was set to 100 m^3/h, and the bypass pipe inlet velocities were set to 10 m/s, 20 m/s, 30 m/s, 40 m/s, and 50 m/s.
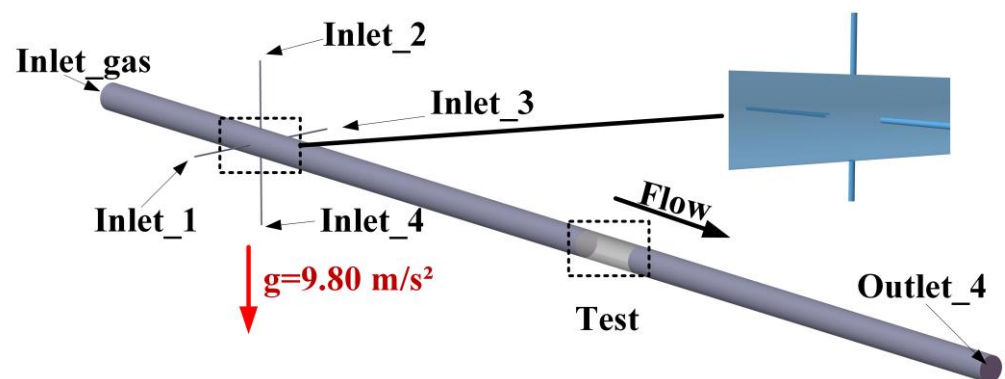
Figure 1. Natural gas pipeline digital model diagram [40].

Table 1. Gas pipeline parameters.

Diameter of Main Pipe (mm)	Main Length (mm)	Length of Bypass Pipe (mm)	Diameter of Bypass Pipe (mm)	Number of Bypass Pipes
100	5000	200	6	4

The standard convergence value is 10^{-6}. The computational fluid shall satisfy the following equation:

Continuity equation:

$$\frac{\partial \rho}{\partial t} + \nabla(\rho \vec{v}) = 0 \tag{1}$$

In this equation, ρ is the fluid density and $\vec{v}$ is the average velocity vector of the mixture.

Momentum equation:

$$\rho \frac{d\vec{v}}{dt} = \nabla \vec{\tau}_{ij} - \nabla p + \rho \vec{F} \tag{2}$$

In this formula, $\overrightarrow{\tau_{ij}}$ is the viscous shear stress and $\overrightarrow{F}$ is the volumetric force.
Energy equation:

$$\rho \frac{dE}{dt} + p\left(\nabla \overrightarrow{v}\right) = \frac{\partial Q}{\partial t} - \nabla \overrightarrow{q} + \overrightarrow{\Phi} \tag{3}$$

In this equation, Q represents the heat source term and $\overrightarrow{\Phi}$ represents the heat dissipation term.
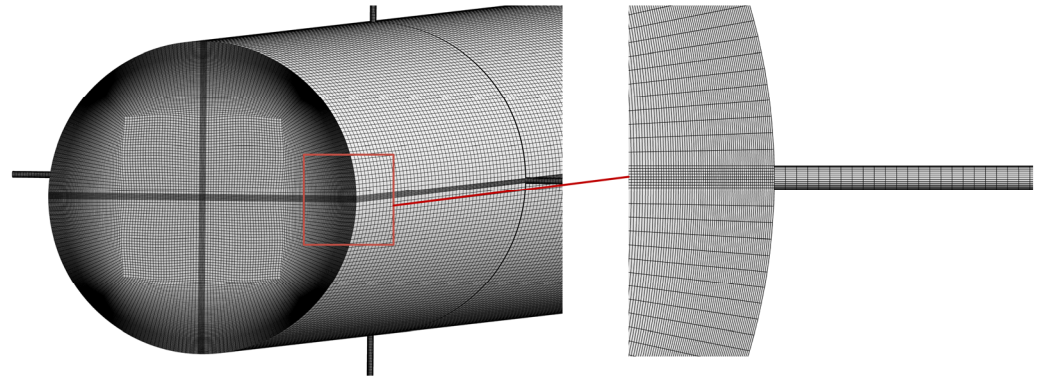
Figure 2. Grid division of bypass pipe in a pipeline.

2.2. Analysis of the Numerical Result

In this numerical simulation, a grid-independent study was conducted by monitoring the exit velocity. As depicted in Figure 3a, when the number of grids exceeded 6×10^6, there was no significant change in velocity with an increasing grid count. Since the actual flow rate of the natural gas pipeline is 3.62 m/s, the grid corresponding to the blue scheme was selected for the numerical simulation. This choice ensures an appropriate balance between computational accuracy and efficiency for the given flow conditions. As depicted in Figure 3b, the velocity distribution inside the pipeline measured by experiment is in good agreement with that by numerical simulation.

Figure 4 represents the relative pressure distribution of the jet flow velocity in the range of 10 to 50 m/s in a bypass pipe. When the jet flow velocity is greater than 20 m/s, there is no coherent jet structure in the symmetric jet flow. Figure 4b shows that even if the jet did not collide, the symmetrical pattern of the cross-flow field was disrupted, and the center of the flow velocity began to deviate from the center axis of the main channel. When the flow rate of the jet is higher than 30 m/s, the jet collides violently in the inner center of the pipe, forming a pair of reverse-rotating re-jet vortices upstream. The reason for this is that the mutual collision of the jets results in the maximum relative pressure occurring at the center of the collision, and the airflow velocity near the center approaches a stagnation point. The airflow then spreads out in all directions, forming a vortex structure. The vortexes appear upstream and downstream of the collision center, with the upstream vortex being significantly larger than the downstream vortex. This is because the jet and cross-flow form a larger recirculation zone upstream, and the downstream vortex dissipates more quickly with the cross-flow velocity field. Moreover, the size of the vortex structure formed by the jet and cross-flow affects the downstream turbulence level. The upstream vortex offset also leads to an increase in the downstream turbulence level. Figure 5 shows the distribution of turbulent kinetic energy inside the pipeline, which increases with an increasing jet flow velocity, and the affected range gradually expands.

(a)

(b)
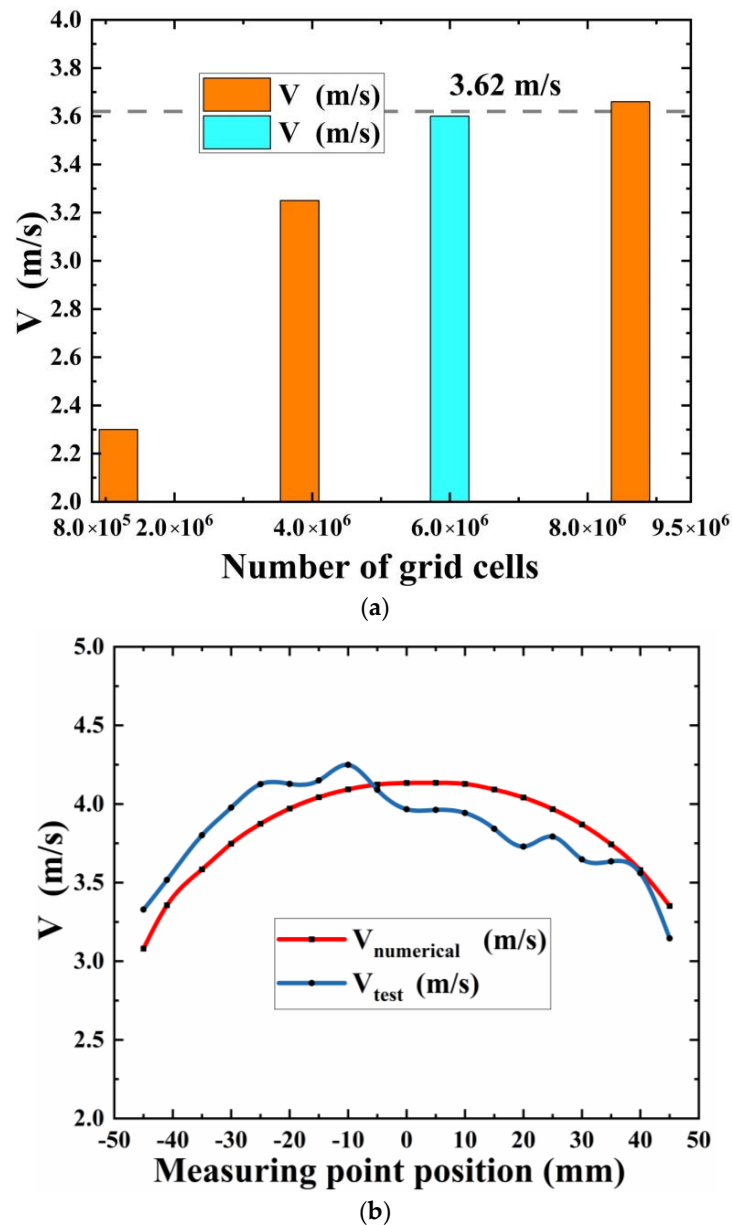
Figure 3. Comparison between the numerical simulation and the experiment. (**a**) Grid independence (the blue one is the selected option). (**b**) Measurement points velocity comparison.

Figure 6 shows the vortex structures under different flow velocities of the jet in a two-dimensional plane based on the Q criterion, including the re-jet vortex, trailing lower vortex, and trailing upper vortex. Figure 7 shows a three-dimensional visualization of the vortex structure. Figure 6 shows that the vorticity increases with an increasing jet flow velocity. The upstream re-jet vortex is the most distinct pair of vortex structures in the flow field. This phenomenon is caused by the mutual collision of jets, which, under the interference and squeezing of the cross-flow, form a re-jet vortex in the upstream part of the jets. With an increasing jet flow velocity, the center position of the vortex structure also migrates upstream. Moreover, even symmetric jet flows can lead to a deviation of the re-jet vortex structure from the center axis of the pipeline. The trailing lower vortex is generated by the jet mixing with the lateral main flow and the mainly low-velocity fluids in the boundary layer near the wall. The trailing upper vortex is generated by the jet wake and migrates downstream with the lateral main flow. When the jet flow velocity is 30 m/s, the vortex structure is located downstream of the jet migrates downward with an increasing

cross-flow. However, with an increasing jet flow, the influence of the downstream vortex structure gradually weakens, while the influence range of the vortex structure increases. The upstream re-jet vortex gradually fills the entire flow channel. Notably, the turbulent kinetic energy and vortex structure exhibit opposite characteristics, because the turbulent region has a higher flow velocity, while a vortex structure is formed due to the rotation of the velocity field. In the flow field of the pipeline, symmetric jets collide with each other, causing the radial velocity of the jets to cancel. There is a strong shear force between the jets and the cross-flow, leading to an increase in the vorticity of the velocity field.
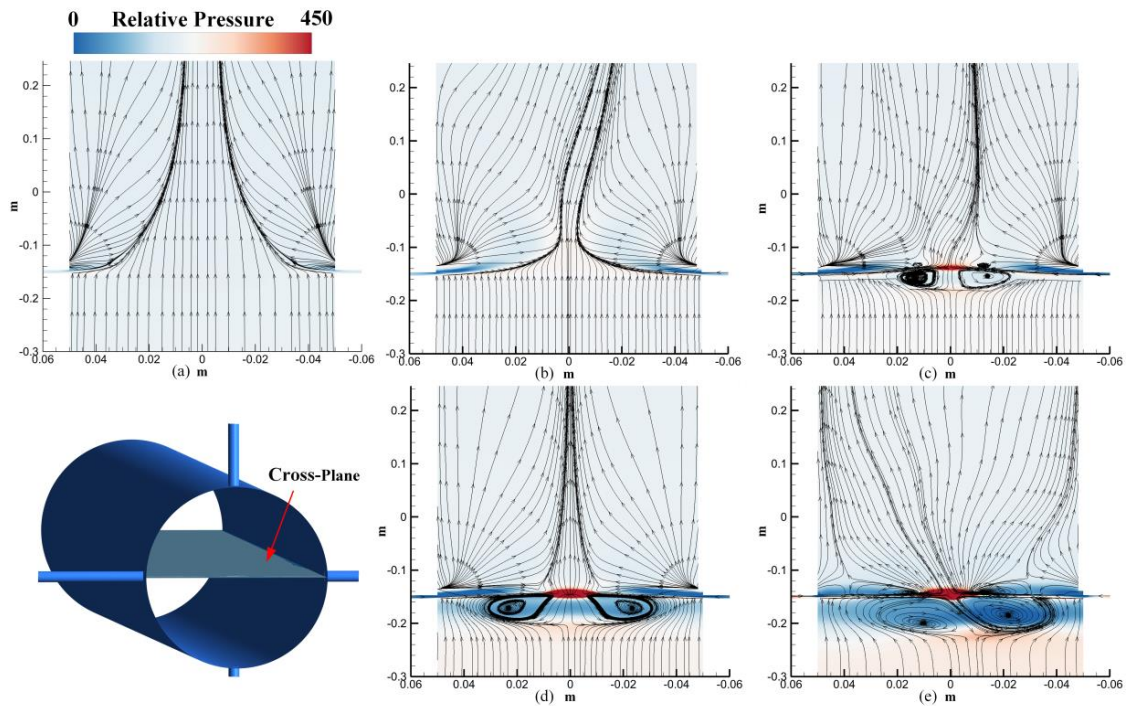
Figure 4. Relative pressure distribution at 10 m/s (**a**), 20 m/s (**b**), 30 m/s (**c**), 40 m/s (**d**), and 50 m/s (**e**).
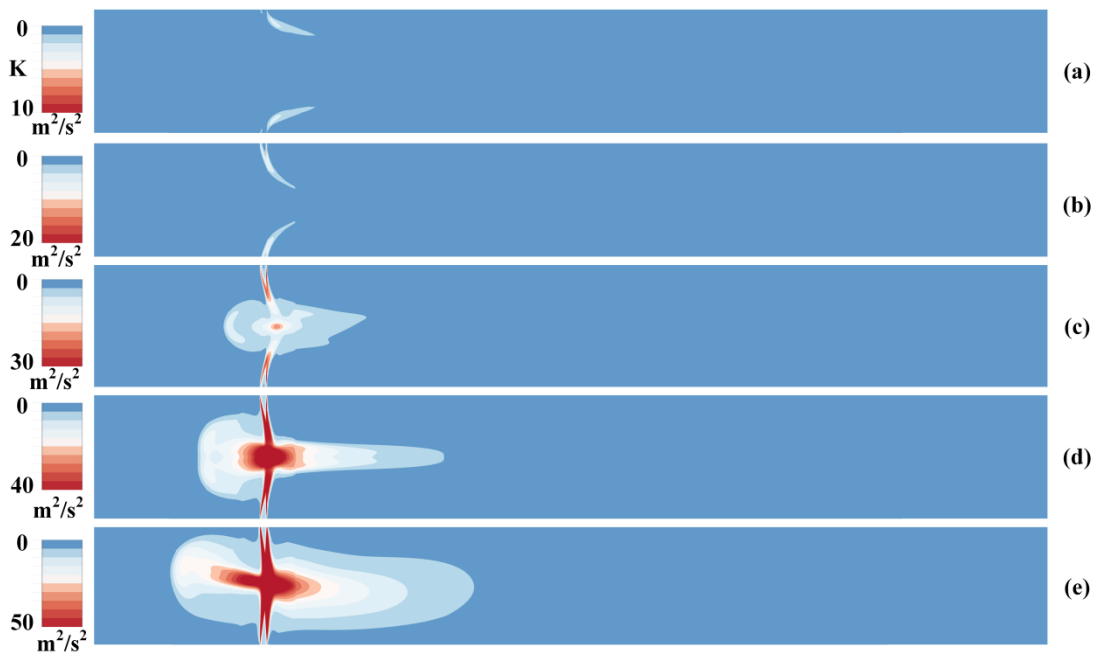
Figure 5. The distribution of turbulent kinetic energy at 10 m/s (**a**), 20 m/s (**b**), 30 m/s (**c**), 40 m/s (**d**), and 50 m/s (**e**).
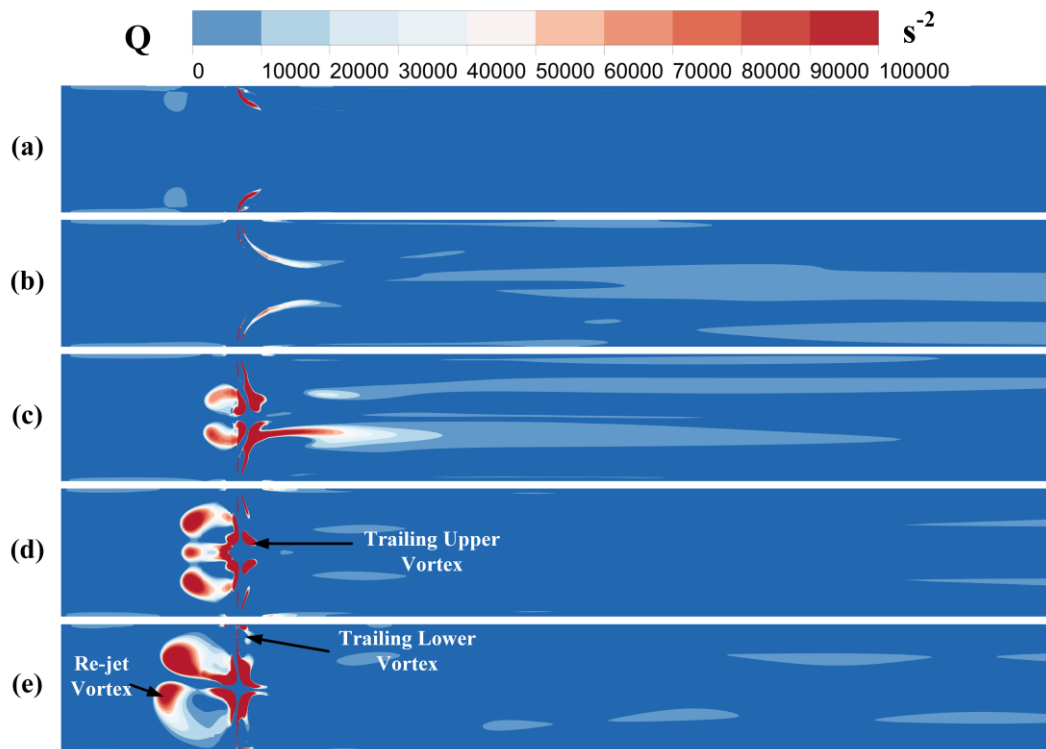
Figure 6. The distribution of the vortex at 10 m/s (**a**), 20 m/s (**b**), 30 m/s (**c**), 40 m/s (**d**), and 50 m/s (**e**).
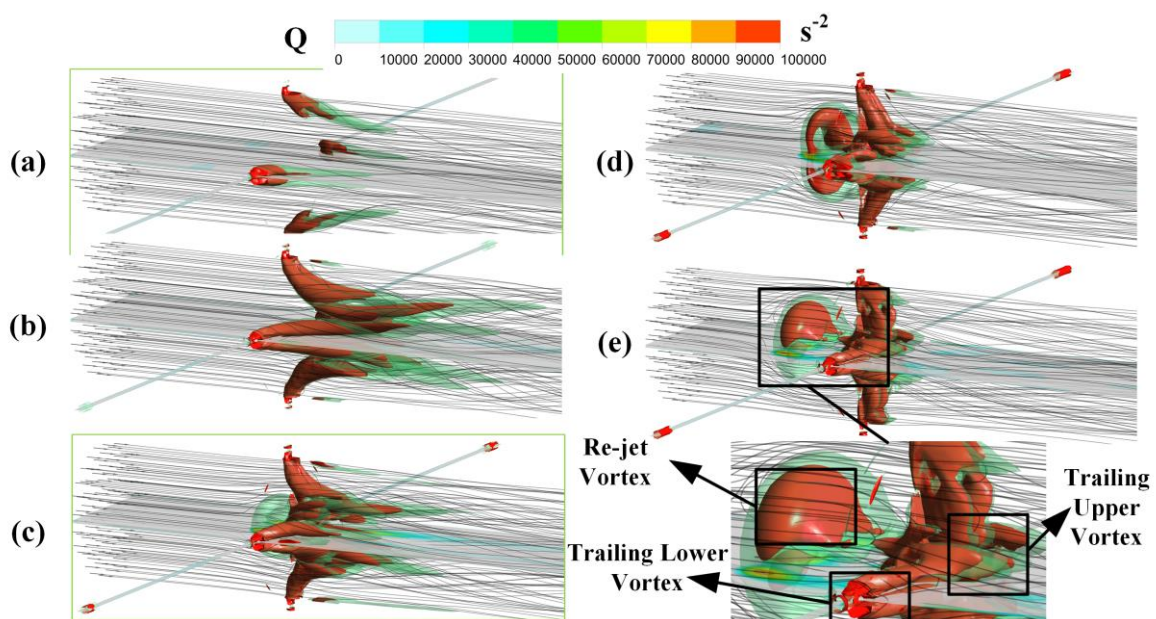
Figure 7. The distribution of the 3D vortex at 10 m/s (**a**), 20 m/s (**b**), 30 m/s (**c**), 40 m/s (**d**), and 50 m/s (**e**).

3. Proper Orthogonal Decomposition

To better analyze and extract data from the symmetric jet flow field, proper orthogonal decomposition is used in this article. The POD method can be used to obtain low-dimensional characteristics of flow fields from large amounts of high-dimensional flow data. Considering the distinct flow characteristics of symmetric jet collisions, three pressure monitoring points are established inside the natural gas pipeline. Fifty snapshots containing flow field features (one transient file every 0.01 s, totaling 0.5 s), were calculated, and

extracted, and POD flow field information extraction was performed. Considering the complex structure and magnanimous space nodes, the snapshot POD method is adopted for its advantages in unsteady flow field analysis. This method is suitable for complex problems, where the number of spatial points M is much greater than the number of sampling time points. The mathematical derivation process is introduced below.

It is supposed that there is a set of observation data matrices that vary with time as follows:

$$X = [x_1 \quad x_2 \quad \cdots x_n] \in R^{m \times n} \tag{4}$$

where *m* represents the size of the spatial domain, and can be used to establish the spatial correlation matrix with Δt:

$$S_{m \times n} = \frac{1}{n} X_{m \times n} X_{m \times n}^T \tag{5}$$

$S_{m \times n}$ is a real symmetric matrix of order $m \times n$, the eigenvalues of which are greater than or equal to 0, with the eigenvectors corresponding to different eigenvalues. The eigenvalues λ and eigenvectors ϕ are solved as follows:

$$S\phi = \lambda\phi \tag{6}$$

The resulting feature vector ϕ_j is the J-order POD mode, and the corresponding time coefficient is:

$$(a_j(t))^T = (X(x,t))^T \phi_j(x) \tag{7}$$

The $r(r > 0)$ nonzero eigenvalues can be further rewritten as follows:

$$\lambda_j = \phi_j^T S(\varphi_j) = \phi_j^T X X^T (\varphi_j) = \left| X^T \varphi_j \right|^2 \tag{8}$$

The eigenvalue is the square of the modulus projected by the original function onto the eigenmode, and its value represents the energy ratio of the mode. The corresponding energy content of each order mode ratio can be expressed as follows:

$$\varepsilon_j = \frac{\lambda_j}{\sum\limits_{j=1}^{n} \lambda_j} \tag{9}$$

3.1. Vortex Distribution Characteristics

In this article, the POD method is used to analyze coherent vortex structures in a jet flow field. Figure 8 shows the energy proportions of modes of order 1–10 at different jet flow rates. At flow rates of 50 m/s and 40 m/s, the first- and second-order modes account for 93.7% and 95.7%, respectively, of the total energy, which is related to the formation of large vortex structures by jet impact. At a 30 m/s jet flow rate, the first- and second-order modes account for 99% of the total energy, and the first-mode energy does not account for more than 85%, as at 50 m/s and 40 m/s, mainly because the symmetrical jets at 30 m/s interfere with each other to form a re-jet vortex. At a flow rate of 20 m/s, the proportion of the mode energy reaches 92.7%. Although the jets do not collide, they interfere with the flow field. At a flow rate of 20 m/s, the energy of each order decreases step by step, and there is no dominant mode. The low-order POD mode represents the large-scale coherent vortex structure of the flow field in the pipeline, and the high-order POD mode represents the small-scale vortex structure of the flow field in the pipeline.

Figure 9a shows the first six orders of the flow velocity at 10 m/s. In Figure 8, the proportion of first-mode energy does not reach 80% or more, as in other percentages. The trailing lower and upper vortexes are the main components of the vortex. The first-order mode mainly manifests as the trailing upper vortex, which exhibits incomplete symmetry. The trailing lower vortex has relatively weak energy, and its detachment has a significant impact on the boundary layer in the downstream flow path. The lower vortex of the

fifth-order mode clearly exhibits regular shedding. Figure 9b shows the first six modes of the flow velocity at 20 m/s. The jet flow has not yet collided, and the main vortex is mainly concentrated in the trailing upper vortex, which is highly concentrated at the tail of the jet flow. Notably, the trailing upper vortex can affect the formation of wall-mounted vortex structures in the boundary layer at certain positions downstream of the nozzle and continue to influence subsequent flow fields.
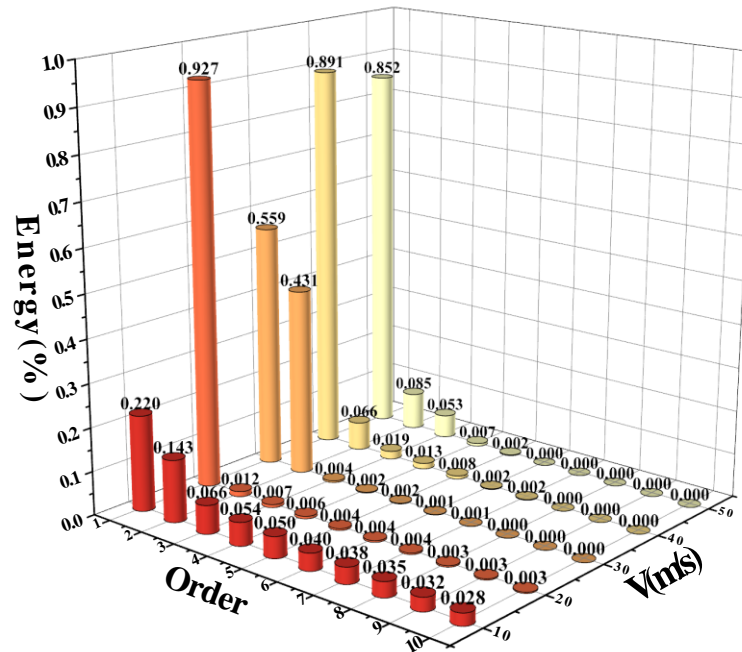
Figure 8. The energy proportion of modes 1–10 at different jet flow velocities.

Figure 10a shows the first six modes at a jet flow rate of 30 m/s. As shown in the figure, the jets collide on the central axis of the pipeline at this time, and the first-order modal diagram shows that an obvious re-jet vortex is formed upstream of the collision center point. Downstream of the nozzle, trailing upper and lower vortexes also form. Based on the energy proportion graph, the energy ratio of the re-jet vortex and trailing upper vortex under the first-order mode reaches 99%. Moreover, many small vortex structures upstream and downstream can be captured on the higher-order modal diagram. Figure 10b shows the first six modes at a jet flow rate of 40 m/s. The first- and second-order modes show the upstream region of the jet hedge center, and the large vortex structure on both sides of the pipeline central axis is consistent with the re-jet vortex in Figure 4e. The first-order mode can clearly capture the existence of trailing upper and lower vortexes, and the energy of the upstream re-jet vortex is concentrated in the jet hedge center. Figure 10c shows the vortex structure of the first six modes at a jet flow speed of 50 m/s. The vortex structure is analyzed by the energy distribution and the structural modal diagram shown. With an increasing jet velocity, the upstream re-jet vortex structure gradually expands, and the downstream vortex structure becomes more concentrated. In the first six modes, the upstream region of the jet hedge center and both sides of the pipeline central axis exhibit a large re-jet vortex structure, which is the main vortex structure upstream. The modes are symmetrical along the central axis, which represents the main vortex structure in the flow field under these conditions. Figure 11 shows the time domain plot of the first three POD mode coefficients. There is a 90-degree phase difference between the first and second modes.
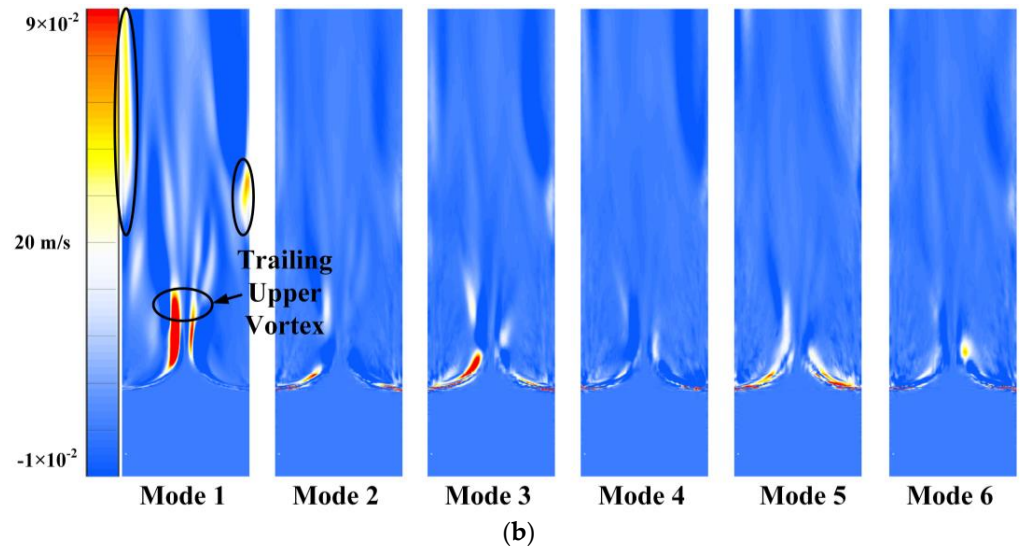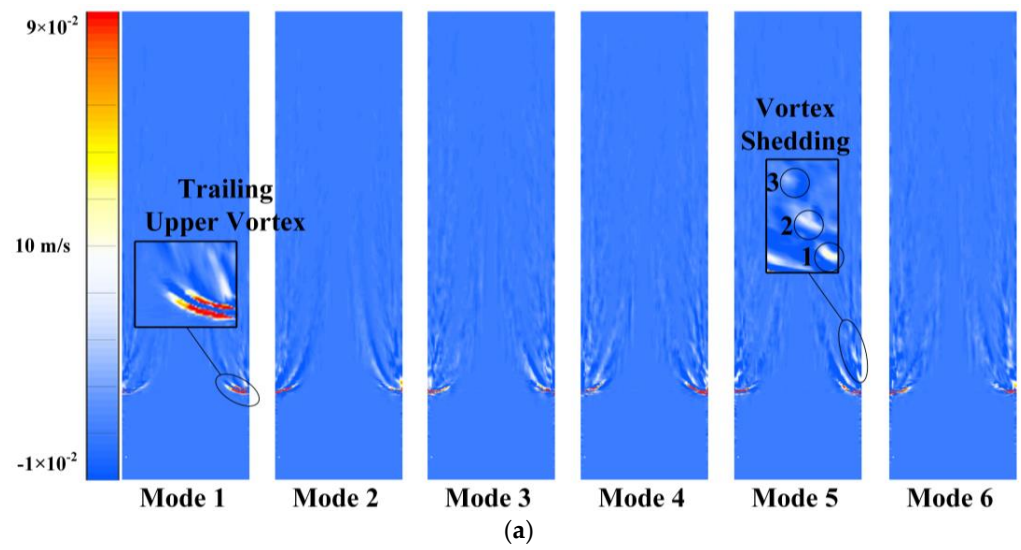
Figure 9. The first six orders at flow rates of 10 m/s (**a**) and 20 m/s (**b**).

Figure 10. *Cont*.

(**b**)

(**c**)
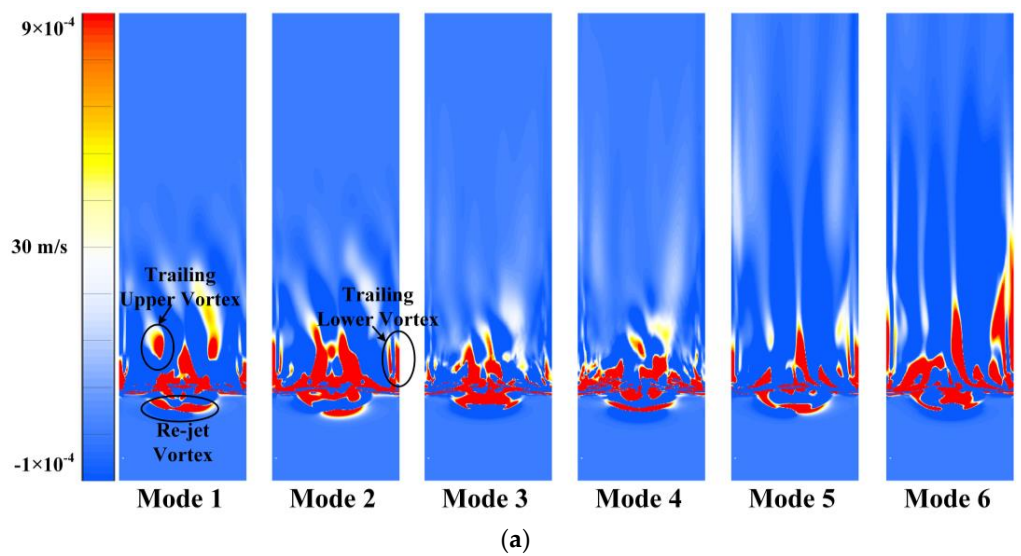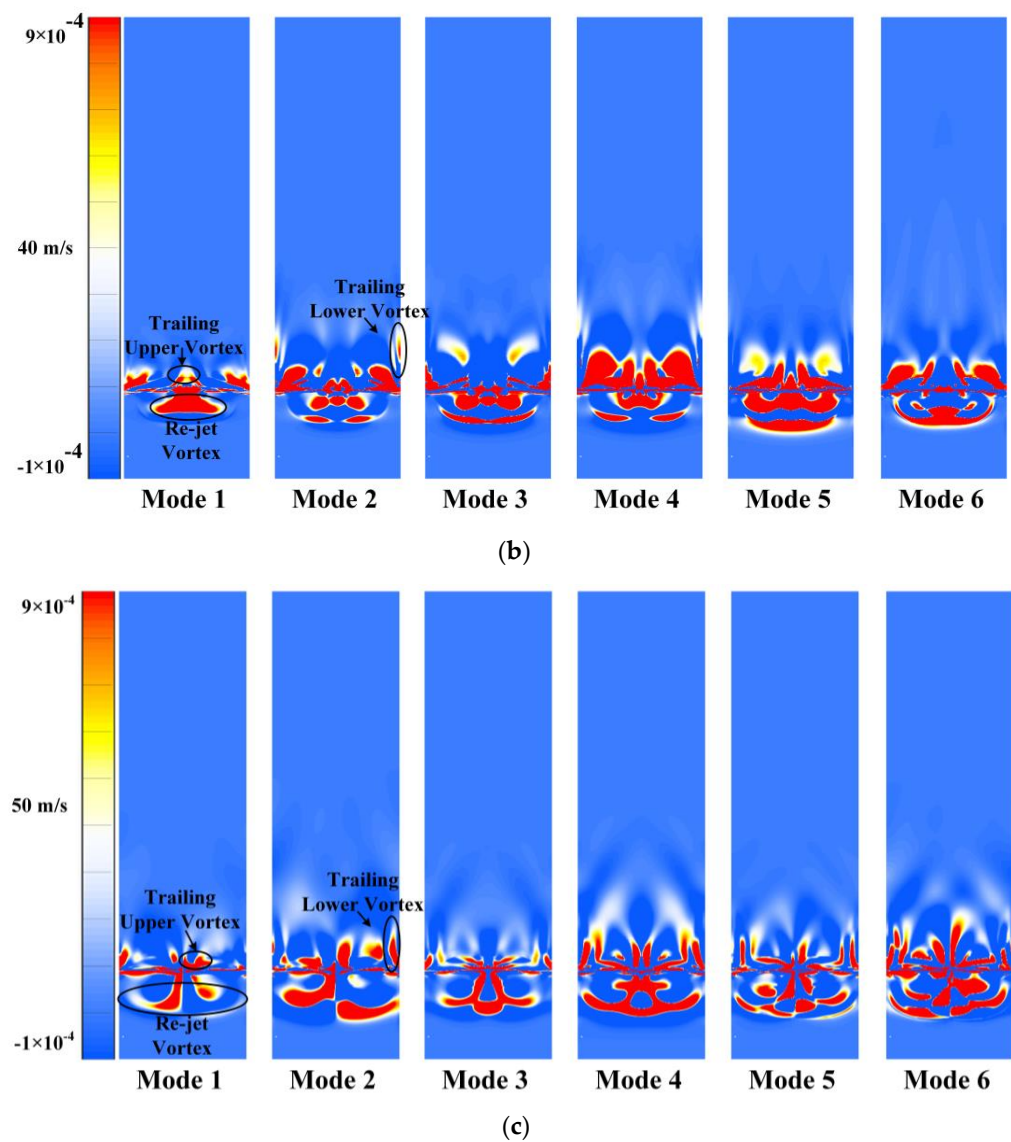
Figure 10. The first six orders at a flow rate of 30 m/s (**a**) 40 m/s (**b**) and 50 m/s (**c**).
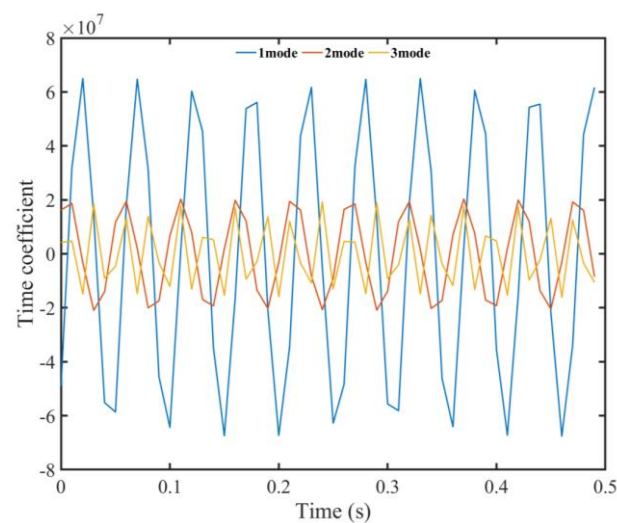
Figure 11. The first six orders at a flow rate of 50 m/s.

3.2. The Result of PIV

Figure 12 is a photograph of the joint test between the Key Laboratory of Fluid and Power Machinery of the Ministry of Education of Xihua University and the Chengdu Branch of the National Oil and Natural Gas Large Flow Metering Station. Figure 13a shows the distribution of tracer particles caused by the injection jet, where the tracer particles are evenly mixed in the pipeline. Figure 13b shows the PIV measurement velocity flow field, which has a uniform velocity distribution and accurate measurement. Therefore, the vortex structure caused by the symmetrical jet filling mode is conducive to ensuring the distribution of tracer particles and improving the snapshot quality of the PIV flowmeter.

Figure 12. The PIV flowmeter for natural gas applications.

| (**a**) | (**b**) |
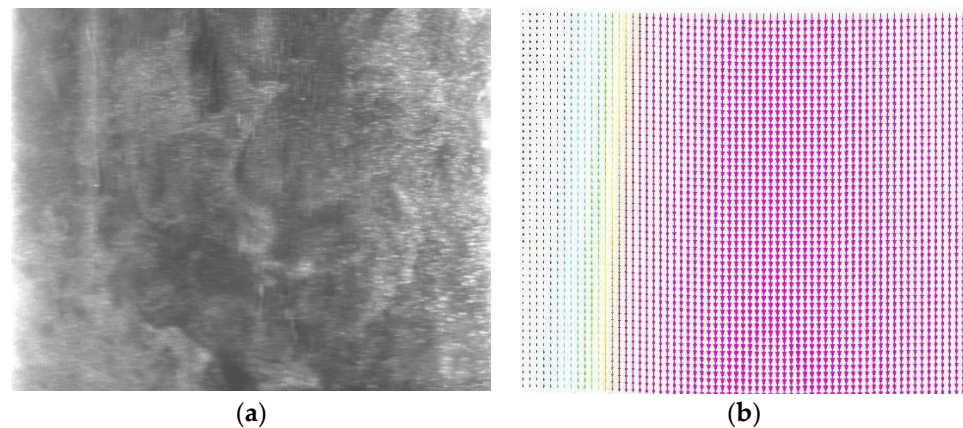
Figure 13. The test of PIV: (**a**) The distribution of tracer particles caused by the injection jet. (**b**) The PIV measurement velocity flow field.

4. Conclusions

The effect of a jet in a pipeline is completely different to that in typical free flow. Gas flowing through the pipeline is predominantly methane, and the flow environment is characterized by high pressure. The flow field within the pipeline is constrained, meaning that both the main flow and the jet streams develop within a limited empty space. As a result, there exists a coherent structure between the jet and the cross flow, which influences the dynamics and behavior of the flow within the pipeline. The main conclusions are as follows:

1.   The jet flow interacts with the crossflow, resulting in the formation of trailing upper and lower vortices. At lower jet flow rates, the trailing upper and lower vortices are located above and below the nozzle, respectively.
2.   As the velocity of the jet flow increases, the trailing upper vortices begin to interfere with each other and gradually merge, forming a re-jet vortex. This observation highlights the complex dynamics and interactions between the jet flow and the surrounding crossflow within the pipeline.
3.   The POD method is employed to analyze the coherent vortex structure in different modes. The first and second order modes exhibit relatively high energy, enabling them to accurately capture the coherent vortex structure of the jet.
4.   Higher order modes are useful for observing and studying the growth and shedding of small-scale vortex structures.
5.   The vortex structure formed by symmetrical jet is conducive to PIV flowmeter measurements.

Author Contributions: Conceptualization, L.L.; writing—original draft preparation, J.L., H.Z. and L.L.; writing—review and editing, Y.Q. All authors have read and agreed to the published version of the manuscript.

Data Availability Statement: The data presented in this study are available in the main text of the article.

Conflicts of Interest: Yilong Qiu was employed by PetroChina Southwest Oil & Gas Field Company. The remaining authors declare that the research was conducted in the absence of any commercial or financial relationships that could be construed as a potential conflict of interest.

References

1.   Neumann, A.; Hirschhausen, C.V. Natural Gas: An Overview of a Lower-Carbon Transformation Fuel. *Rev. Environ. Econ. Policy* **2015**, *9*, 64–84. [CrossRef]
2.   Wu, X.; Wang, Z.; Dong, M.; Dong, L.F.; Ge, Q. A Critical Analysis of Natural Gas Liquefaction Technology. *Fluids Dyn. Mater. Process.* **2022**, *18*, 145–158. [CrossRef]
3.   Kuang, Y.; Lin, B. Unwatched Pollution Reduction: The Effect of Natural Gas Utilization On Air Quality. *Energy* **2023**, *273*, 127247. [CrossRef]
4.   Kuang, Y.M.; Lin, B.Q. Natural Gas Resource Utilization, Environmental Policy and Green Economic Development: Empirical Evidence From China. *Resour. Policy* **2022**, *79*, 102992. [CrossRef]
5.   Li, W.; Lu, C. The Multiple Effectiveness of State Natural Gas Consumption Constraint Policies for Achieving Sustainable Development Targets in China. *Appl. Energy* **2019**, *235*, 685–698. [CrossRef]
6.   Jia, A.; Cheng, G.; Chen, W.; Li, Y. Forecast of natural gas supply and demand in China under the background of "Dual Carbon Targets". *Pet. Explor. Dev.* **2023**, *50*, 492–504. [CrossRef]
7.   Liu, H.; Liu, Y.; Wang, C.; Song, Y.; Jiang, W.; Li, C.; Zhang, S.; Hong, B. Natural Gas Demand Forecasting Model Based On Lasso and Polynomial Models and its Application: A Case Study of China. *Energies* **2023**, *16*, 4268. [CrossRef]
8.   Ou, J.; Chen, Y. A Novel Dynamic Parameter Discrete Grey Model and its Application. *Energy Rep.* **2023**, *9*, 4941–4950. [CrossRef]
9.   Jenkins, C.M.; Horie, Y.; Wu, C.Y. Particle Velocity and Structures in Blast Waves Imaged Using Particle Image Velocimetry. *Int. J. Multiph. Flow* **2010**, *36*, 88–91. [CrossRef]
10. Gao, Q.; Wang, H.; Shen, G. Review On Development of Volumetric Particle Image Velocimetry. *Chin. Sci. Bull.* **2013**, *58*, 4541–4556. [CrossRef]
11. Liu, S.; Xu, J.; Gong, H.; Yu, K. Experimental Comparison of Piv-Based Pressure Measurements in Supersonic Flows with Shock Waves. *Meas. Sci. Technol.* **2019**, *30*, 105201. [CrossRef]
12. Li, W.; Li, Z.; Deng, W.; Ji, L.; Qiu, Y.; Chen, H. Particle Image Velocimetry Flowmeter for Natural Gas Applications. *Flow Meas. Instrum.* **2021**, *82*, 102072.
13. Ranz, W.E. Some Experiments On Orifice Sprays. *Can. J. Chem. Eng.* **1958**, *36*, 175–181. [CrossRef]
14. Atmaca, M.; Cetin, B.; Ezgi, C.; Kosa, E. CFD Analysis of Jet Flows Ejected From Different Nozzles. *Int. J. Low-Carbon Technol.* **2021**, *16*, 940–945. [CrossRef]
15. Muhammad, N.; Alharbi, K.A.M. OpenFOAM for Computational Hydrodynamics Using Finite Volume Method. *Int. J. Mod. Phys. B* **2023**, *37*, 2350026. [CrossRef]

16. Rehman, S.; Muhammad, N. Mathematical Analysis of Nonlinear Models and their Role in Dynamics. *Mod. Phys. Lett. B* **2023**. [CrossRef]
17. Cao, W.; Altoum, S.H.; Othman, H.A.; Alzubaidi, A.M.; Alghawli, A.S. Numerical Modeling for Thermal Behavior of Nanomaterial Laminar Flow and Convective Heat Transfer in Appearance of Magnetic Field. *Case Stud. Therm. Eng.* **2023**, *42*, 102727. [CrossRef]
18. Upadhyay, P.; Valentich, G.; Kumar, R.; Alvi, F. Flow and Acoustic Characteristics of Non-Axisymmetric Jets at Subsonic Conditions. *Exp. Fluids* **2017**, *58*, 52. [CrossRef]
19. Xiao, S.; Ge, Z.; Ren, Q.; Liu, J.; Wang, H. Numerical Analysis On the Flow Field Structure and Deflection Characteristics of Water Jets Under Nozzle Moving Conditions. *Eng. Appl. Comp. Fluids* **2020**, *14*, 1279–1301. [CrossRef]
20. Cai, C.; Ren, K.; Li, Q. Numerical Simulation of the Flow Field Structure of Liquid Nitrogen Jet. *Therm. Sci.* **2019**, *23*, 1337–1343. [CrossRef]
21. Bi, R.; Ali, S.; Savory, E.; Zhang, C. A Numerical Modelling Investigation of the Development of a Human Cough Jet. *Eng. Comput.* **2022**, *39*, 773–791. [CrossRef]
22. Hou, R.; Huang, C.; Zhu, H. Numerical Simulation Ultrahigh Waterjet (Wj) Flow Field with the High-Frequency Velocity Vibration at the Nozzle Inlet. *Int. J. Adv. Manuf. Tech.* **2014**, *71*, 1087–1092. [CrossRef]
23. Lee, C.; Ozawa, Y.; Haga, T.; Nonomura, T.; Asai, K. Comparison of Three-Dimensional Density Distribution of Numerical and Experimental Analysis for Twin Jets. *J. Vis.* **2021**, *24*, 1173–1188. [CrossRef]
24. Hart, J.T.; Karim, M.R.; Bhuiyan, A.A.; Witt, P.; Naser, J. Numerical Modelling of Unsteady Flow Behaviour in the Rectangular Jets with Oblique Opening. *Alex. Eng. J.* **2016**, *55*, 2309–2320. [CrossRef]
25. Miltner, M.; Jordan, C.; Harasek, M. CFD Simulation of Straight and Slightly Swirling Turbulent Free Jets Using Different Rans-Turbulence Models. *Appl. Therm. Eng.* **2015**, *89*, 1117–1126. [CrossRef]
26. Zheng, J.X.; Wang, X.K.; Tan, D.S.; Tan, S.K. Experimental Investigation of Interactions of Three Co-Planar and Converging Jets. *Exp. Fluids* **2014**, *55*, 1733. [CrossRef]
27. Afzal, A.; Ansari, Z.; Faizabadi, A.R.; Ramis, M.K. Parallelization Strategies for Computational Fluid Dynamics Software: State of the Art Review. *Arch. Comput. Methods Eng.* **2017**, *24*, 337–363. [CrossRef]
28. Dai, Y.; Zhang, Y.; Li, X. Numerical and Experimental Investigations On Pipeline Internal Solid-Liquid Mixed Fluid for Deep Ocean Mining. *Ocean Eng.* **2021**, *220*, 108411. [CrossRef]
29. Kang, H.; Tian, Z.; Chen, G.; Li, L.; Wang, T. Application of Pod Reduced-Order Algorithm On Data-Driven Modeling of Rod Bundle. *Nucl. Eng. Technol.* **2022**, *54*, 36–48. [CrossRef]
30. Lee, S.J. Pod Analysis of Near-Wake Structures of an Elliptic Cylinder Adjacent to a Free Surface. *J. Vis.* **2004**, *7*, 179–186.
31. Sakai, M.; Sunada, Y.; Imamura, T.; Rinoie, K. Experimental and Numerical Studies on Flow behind a Circular Cylinder Based on POD and DMD. *Trans. Jpn. Soc. Aeronaut. Space Sci.* **2015**, *58*, 100–107. [CrossRef]
32. El-Adawy, M.; Heikal, M.R.; Aziz, A.R.A.; Adam, I.K.; Ismael, M.A.; Babiker, M.E.; Baharom, M.B.; Firmansyah; Abidin, E.Z.Z. On the Application of Proper Orthogonal Decomposition (Pod) for in-Cylinder Flow Analysis. *Energies* **2018**, *11*, 2261. [CrossRef]
33. Zhang, Y.; Vanierschot, M. Proper Orthogonal Decomposition Analysis of Coherent Motions in a Turbulent Annular Jet. *Appl. Math. Mech.* **2021**, *42*, 1297–1310. [CrossRef]
34. Jang, Y.I.; Lee, S.J. Pod Analysis On the Sphere Wake at a Subcritical Reynolds Number. *J. Vis.* **2010**, *13*, 311–318. [CrossRef]
35. Deep, D.; Sahasranaman, A.; Senthilkumar, S. POD Analysis of the Wake Behind a Circular Cylinder with Splitter Plate. *Eur. J. Mech. B Fluids* **2022**, *93*, 1–12. [CrossRef]
36. Wang, M.; Cao, S.; Cao, J. POD-Based Analysis of Time-Resolved Tornado-Like Vortices. *Wind Struct.* **2021**, *33*, 13–27.
37. Wu, W.; Zhou, C. A Numerical Study of the Tip Wake of a Wind Turbine Impeller Using Extended Proper Orthogonal Decomposition. *Fluid Dyn. Mater. Process.* **2020**, *16*, 883–901. [CrossRef]
38. Apacoglu, B.; Paksoy, A.; Aradag, S. CFD Analysis and Reduced Order Modeling of Uncontrolled and Controlled Laminar Flow Over a Circular Cylinder. *Eng. Appl. Comput. Fluid Mech.* **2011**, *5*, 67–82. [CrossRef]
39. Sen, U.; Mukhopadhyay, A.; Sen, S. Effects of Fluid Injection on Dynamics of Flow Past a Circular Cylinder. *Eur. J. Mech. B Fluids* **2017**, *61*, 187–199. [CrossRef]
40. Chen, H.; Qiu, Y.; Wang, H. Numerical and Experimental Investigation of Flow Characteristics in Natural Gas Pipe. *AIP Adv.* **2023**, *13*, 045017. [CrossRef]